Journal of Wind Engineering & Industrial Aerodynamics 188 (2019) 207–216

Contents lists available at ScienceDirect

Journal of Wind Engineering & Industrial Aerodynamics

journal homepage: www.elsevier.com/locate/jweia

# The influence of reduced Reynolds number on the wake of the DrivAer estate vehicle

T. Avadiar *, M.C. Thompson, J. Sheridan, D. Burton

*Department of Mechanical and Aerospace Engineering, Monash University, Melbourne, 3800, Australia*

ARTICLE INFO

*Keywords:*
Automotive aerodynamics
Wind tunnel
Bluff body
Wake
Transient
Reynolds number

ABSTRACT

Experiments on vehicle aerodynamics were conducted in a low-speed water channel at a Reynolds number two orders of magnitude lower than that of typical full-scale studies. Particle Image Velocimetry (PIV) measurements, focused on the wake of a realistic estate passenger vehicle model, were obtained and compared with existing wake measurements from full-scale wind-tunnel tests. The combination of sharp and rounded trailing edges present on the geometry impacts properties of the separating shear layers, although the general wake structures are qualitatively similar. In both cases, the wake remains dominated by the upwash from the underbody exit diffuser outflow. Effects of the reduced Reynolds number on the spectral content of the wake velocity field downstream of the recirculation region are also documented.

## 1. Introduction

Increased operational numbers of passenger vehicles worldwide have required continued efforts to reduce their energy usage because of environmental concerns and for economic benefits. The aerodynamic drag contributes approximately 60% of the overall resistive force for an estate vehicle operating at highway speeds (Heft et al., 2012).

Pressure drag dominates the overall aerodynamic drag contribution of passenger vehicles, which leads to drag reduction strategies focusing on the flow structures around and at the rear of a vehicle. This requires an understanding of the time-averaged and dynamic properties of the highly vortical flows, especially in the vehicle's wake. To elucidate these complex interactions, full-scale vehicle experiments and high fidelity transient numerical simulations are generally considered the best options. Although the availability of wind-tunnel facilities has increased, they often still remain limited in their capability to capture the wake dynamics of full-size vehicles.

Capturing time-accurate data at full-scale Reynolds numbers often demands direct in-flow measurements, sampling at frequencies much higher than those associated with vortex shedding. Reduced Reynolds number experiments, such as those performed in a low-speed water channel, can lead to improved spatial resolution when using time-resolved Particle Image Velocimetry (PIV). The required sampling frequency is therefore achieved, allowing the important spatial and temporal dynamics of the wake to be captured.

Modern estate vehicles and their variants possess geometries with a combination of sharp edges with defined separation and larger radius edges, in contrast to simplified models, such as the Ahmed, Windsor or GTS geometries, with only sharp trailing edges. Spohn and Gillieron (Williamson, 1996) found the wake structures of the Ahmed model are similar over a Reynolds number range of two orders of magnitude. As the Reynolds number is increased, the flow regimes over curved surfaces such as bumpers and pillars change from separation at the shoulder to a downstream detachment point, associated with a laminar separation bubble as outlined by Williamson (1996). This results in the shear layers advecting more energy into the wake, resulting in greater pressure recovery at the base. Of interest, is the influence of reduced Reynolds number testing on the flow around curved trailing edges when the approaching upstream boundary layer is turbulent, such as for BLs found on automotive vehicles.

More complex, partially de-featured, bluff-body wakes with curved or slanted trailing edges may be inherently more sensitive to changes in Reynolds numbers. Work by Venning et al. (2017) found flow separation over the top of an Ahmed 25° slant body influenced by viscous effects, with increased downwash and momentum for the full-scale studies by Lienhart (Lienhart et al., 2002). Venning et al. also found that the large-scale flow structures were still seen in the reduced-scale experiments. Furthermore, Spohn and Gilliéron (Spohn and Gilliéron, 2002) utilised flow visualisation ($Re \approx 10^4$) to show that the wake is similar to studies conducted at a Reynolds number 2 orders of magnitude higher

* Corresponding author.
*E-mail address:* terence.avadiar@monash.edu (T. Avadiar).

https://doi.org/10.1016/j.jweia.2019.02.024
Received 29 September 2018; Received in revised form 26 February 2019; Accepted 26 February 2019
Available online 12 March 2019

(Re ≈ $10^6$). A study of curved trailing edges on an axisymmetric body by Buresti (Buresti et al., 1997) found varying local radii resulted in a different base pressure distribution for two wind speeds tested. Low Reynolds number experiments on a simplified cyclist by Barry et al. (2016) found key drag-causing flow structures were representative of those at full-scale observed in a wind tunnel. However, they also found smaller-scale salient structures, whose relative scales are not dissimilar to those from shedding off wing-mirrors and wheels, which may dissipate more quickly at the reduced Reynolds number.

This paper examines differences in the wake of a realistic estate vehicle at two Reynolds numbers (≈ $10^5$ and $10^7$), comparing lower Reynolds number water channel results to previously published full-scale wind-tunnel results (Avadiar et al., 2018). In particular, properties of the separating shear layers at the top and sides of the rear surface of the vehicle are compared. Lastly, the differing spectral contents of the wake downstream of the spoiler trailing edge are compared to highlight the impact of Reynolds number on the breakdown of time-averaged wake vortices. Indeed, the reduced Reynolds number wake shows a semi-quantitative similarity to the full-scale case. Because of the relative ease of obtaining PIV fields in water relative those at full-scale in a wind-tunnel (smaller, cheaper lasers, slower flow speeds) this allows for a more detailed analysis of the wake within the recirculation region when coupled with results from full-scale studies.

## 2. Experimental setup

Experiments were conducted in two facilities: a large wind tunnel (WT) and a water channel (WC) at Monash University. Facility and model properties such as the test section dimensions, model details, associated flow qualities and Reynolds numbers tested at are provided and discussed in the relevant sub-sections below.

### 2.1. Full-scale testing - wind tunnel

The full-scale wake surveys were obtained from the 1.4 MW large wind tunnel of the Monash Wind Tunnel Platform (MWTP), assembling results from a previous study (Avadiar et al., 2018). The test section is a 3/4 open-jet closed-loop wind tunnel with working dimensions of 12 × 4 × 2.6 $m^3$ ($L \times W \times H$). The highest attainable free-stream velocity is 55 $ms^{-1}$, with a turbulence intensity of $I_{UVW} \leq 1.6\%$. A (moving) ground simulation system was not available. Experiments were conducted at 28 $ms^{-1}$, or approximately 100 $kmh^{-1}$, with a Reynolds number (based on vehicle length) of $Re_{L,WT} = 8 \times 10^6$.

The DrivAer estate vehicle measures 4.61 × 1.82 × 1.42 $m^3$ ($L \times W \times H$), with a frontal area (FA) of 2.16 $m^2$. This represents a blockage ratio of 20.7%. Mercker's two-gradient modification to open-jet drag corrections were employed to correct the raw (Avadiar et al., 2018) drag measurements. The model was configured with the estate top/rear, wing mirrors and a smooth underbody. Solid wheels with rubber patches minimized the effects of ride height and attitude variance associated with pneumatic tires.

Force measurements obtained in the MWTP tunnel from the previous study (Avadiar et al., 2018) were found to be in good agreement with other published values. Furthermore, the pressure profile along the vehicle's centreline was found to replicate the same trends, with an offset in magnitudes relative to moving ground and a static ground simulation with boundary layer control active.

#### 2.1.1. Velocity and base pressure measurements

Velocities were measured using 4-hole dynamic pressure probes (commercially known as (TFI) *Cobra* probes (Mousley, 2011)), mounted on an automated traverse system. The sampling rate was chosen as 1 kHz for the *Cobra* probe measurements. An acquisition time of 40 s was chosen to ensure that at least ~ 150 shedding cycles were obtained based on an assumed shedding frequency of $St_{\sqrt{FA}} = 0.2$. The *Cobra* probe is able to resolve the three velocity components of incoming flow provided the velocity vector lies within an incidence cone of 45° (Mousley, 2011). Due to this limited acceptance cone of *Cobra* probes, time-averaged velocity profiles presented require a minimum of 80% of acceptable data, falling within the probe's calibration surface, similar to work presented by Li et al. (2017). Transient results presented had a minimum of 95% acceptable data. The reduced acceptance level for time-averaged profiles may result in slightly different velocity magnitudes due to aliasing and a decreased number of samples. However, the sampling time period was chosen in order to minimise these effects and produce the same trends for the transient and time-averaged measurements.

Velocities previously published (Avadiar et al., 2018) using the *Cobra* probe were obtained at various longitudinal distances of $X/H = 0$, 0.25, 0.5, 0.75, 0.9 and 1 along the vehicle centreline, as shown in Fig. 1. The separated shear layers off the bumper, tail-lights and D-pillar respectively were also measured at the corresponding heights of $Z/H = 0.3$, 0.5 and 0.8. Two transverse planes ($yz$) at the longitudinal distances of $X/H =$ 0.5 and 1 were additionally sampled.

Base pressure measurements originally presented in (Avadiar et al., 2018) were captured from 120 locations, sampled simultaneously using a 128 channel *Dynamic Pressure Measurement System* manufactured by *Turbulent Flow Instrumentation*. Pressures were sampled at 1000 Hz for 600 s. Amplitude and phase distortion corrections were applied for the 1500 mm long tubing, allowing frequencies of up to 150 Hz to be resolved. Results accounted for horizontal buoyancy effects by applying a static pressure factor from the base location to an upstream reference Pitot-static tube, measured in the empty wind-tunnel configuration.

### 2.2. Reduced scale testing - water channel

Experiments presented here were conducted at the *Fluid Laboratory for Aerodynamics and Industrial Research* (FLAIR) water-channel facility. The test section measures 4 × 0.6 × 0.8 $m^3$ ($L \times W \times H$), with a turbulence intensity of 0.5%. The channel was set to a water depth set of 0.78 m, resulting in a freestream velocity of 0.45 $ms^{-1}$, and an equivalent length-based Reynolds number of $Re_{L,WC} = 115,000$.

The geometry used is a 1:20 scale DrivAer model, machined from ureol with its detailed wheels and wing mirrors 3D printed. Geometric details with local radii of up to 0.25 mm (equivalent to 5 mm full-scale) were replicated, allowing for door handles, wheel grooves and inverse radii, such as passenger window recesses to be conserved. The model was fixed through the wheel contact patches to a false floor. The assembly was mounted upside down, with the ground plane being 0.25 m below the mean free surface height. The false floor was a clear acrylic ground plane, with a 4:1 elliptical profile at the leading edge to prevent separation. The DrivAer model's nose is located 2.2$H$ downstream from the leading edge of the false floor elliptical nose.

A CAD depiction of the vehicle model and ground plane is shown in Fig. 2 utilising the same reference coordinate system as was deployed for the full-scale experiments.

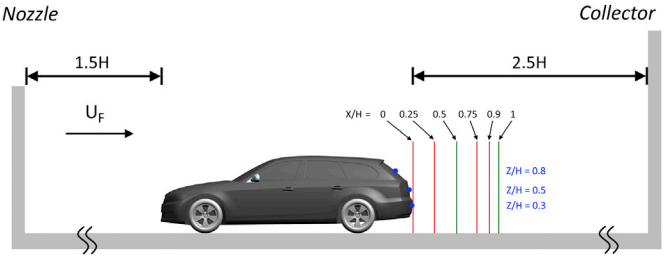


**Fig. 1.** Experimental setup and longitudinal position of the DrivAer estate relative to the wind tunnel test section. Streamwise locations indicating single-axis measurements are shown. At $X/H = 0.5$ (green line), a $yz$ or transverse plane was additionally measured. (For interpretation of the references to colour in this figure legend, the reader is referred to the Web version of this article.)

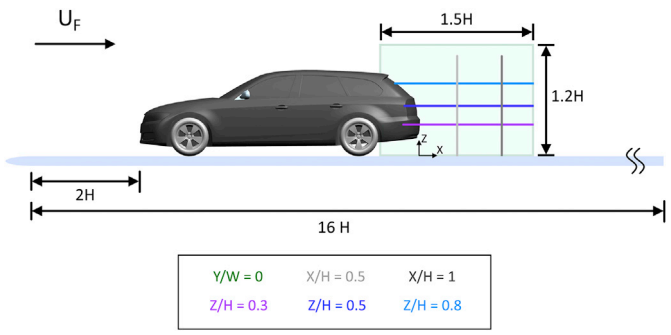


**Fig. 2.** Experimental setup of the 1:20 scale DrivAer estate with a false floor. The locations and sizes of the streamwise, horizontal and transverse PIV planes sampled are provided and scaled relative to the vehicle.

#### 2.2.1. PIV techniques

Velocity in the longitudinal ($xz$), horizontal ($xy$) and transverse ($yz$) planes were measured using Time-Resolved (TR) planar PIV. Survey locations correspond to data available from the full-scale experiments, shown in Fig. 2.

The flow is illuminated by a 5 W, 532 nm continuous laser, passing through a cylindrical glass lens to create a planar light sheet with a thickness of $\approx 1$ mm or $0.012H$. Flow is seeded with spherical glass bubbles (Vestosint) with a mean diameter of 56 $\mu$m and a density of 1.016 kg/m$^3$. Images are sampled with a PCO Dimax.S4 CMOS camera with $2016 \times 2016$ resolution, at a sampling frequency of 300 Hz, corresponding to a non-dimensional frequency of $\mathrm{St} = f(FA)/U_{F,WC} \simeq 3.6$. Multiple sets of data for each plane were captured to ensure that at least $\sim 120$ $St_{\sqrt{FA}} = 0.2$ shedding cycles were obtained, approximately matching the equivalent non-dimensional recording time of the wind-tunnel measurements.

Velocity vectors were obtained using correlation windows of $32 \times 32$ pixels, with 50% overlap. The final spatial resolution for the velocity fields provided was $0.01H$ for the longitudinal ($xz$) and horizontal ($xy$) planes, and $0.015H$ for the transverse ($yz$) plane. Uncertainty analysis using techniques outlined by Raffel et al. (2007) and Wieneke et al. (Wieneke, 2015) for the velocity measurements, was undertaken based on velocity gradients in the shear layers downstream of where vortex roll-up was found to occur. The estimated uncertainty included contributions from the interrogation algorithm, image quality, particle properties and optics. Maximum errors of 6% for the longitudinal ($xz$) and horizontal ($xy$) planes, and 8% for the transverse ($yz$) plane were estimated.

### 2.3. Ground boundary layer

The wind tunnel and water channel results presented utilised a stationary floor. Of some interest are the heights of the ground boundary layer (BL), measured along the vehicle centreline. BL heights at the front of the vehicle are compared in Fig. 3. The thicker BL present at the reduced-scale exhibits a more laminar profile, with the displacement and momentum thickness being 34% and 20% thicker respectively than the full-scale ground boundary layer. The resultant deficit in momentum is expected to reduce the underbody velocity magnitude for the reduced-scale case and this is addressed further in the results section.

As with the published full-scale results, it is expected that an increased ground BL may change the strength of flow structures, but the wake flow topology would remain similar. Ultimately, the wake topology of reduced-scale experiments includes the influence of an augmented BL development and underbody flow changes.

## 3. Results

Presented below are the time-averaged and transient properties of wake velocity measurements. Each section outlines the differences, similarities and provides insights into the wake to complement existing full-scale measurements.

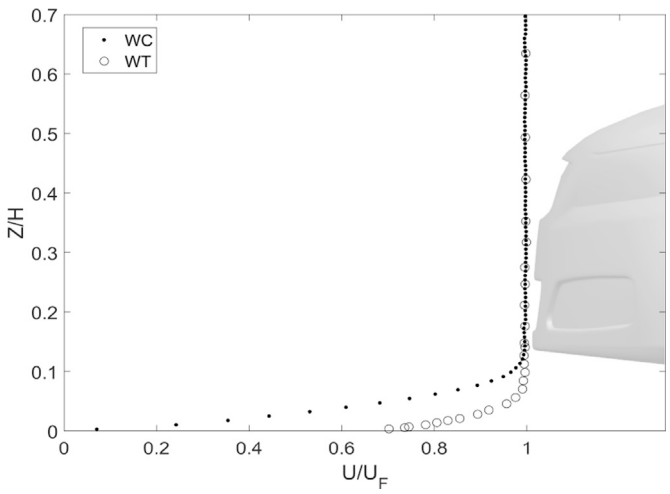


**Fig. 3.** Empty facility boundary-layer profiles at the nose of the estate vehicle for the reduced regime (WC) and full-scale experiments (WT). The vehicle silhouette, correctly scaled, is provided as a geometric reference for the measured BL heights and shapes.

### 3.1. Time-averaged velocity profiles

The centreline velocity profiles in Figs. 4 and 5 show similar trends despite the distinctly different Reynolds numbers. Of interest, the upwash and downwash in the wake, a consequence of underbody outflow and separated flow off the roof, have similar convection levels toward the centreline. The location of maximum streamwise velocity at the underbody outflow increases vertically at the same rate for both cases. Downstream of $X/H = 0.75$, the streamwise and vertical components appear to reach self-similarity for each case. Additionally, the vertical location of maximum streamwise velocity, $U/U_F$, from the underbody exit increases in both cases from $X/H = 0.75$ to $X/H = 0.9$, and remains at the same height at $X/H = 1$. The vertical velocity, $W/U_F$, profiles indicate a similar trend, with both flow states dominated by upwash.

The significantly reduced Reynolds number introduced an increased ground BL thickness leading up to the vehicle, effectively causing significant blockage between the vehicle and ground. On this point, Castelain et al.'s (Wieneke, 2015) work with uniform underbody blockage for a simplified truck found the base pressure distribution was unaffected for reduced underbody exit flows of up to 65% of the baseline. In addition, McArthur et al. (2016) found reduced ground clearances of up to 40% of the baseline configuration resulted in little change to the near-wake topology of a simplified truck. In this study, the ratio of displacement thicknesses and maximum underbody exit velocities between the two Reynolds number regimes presented were $\delta^*_{WT}/\delta^*_{WC} = 0.67$ and $U_{WC}/U_{WT} = 0.7$. Given the findings for (square-back) trucks, the effective ground clearance change and the reduction in underbody velocity are not expected to significantly change the time-averaged near-wake topology between the two regimes.

The streamwise velocity of the separated roof flow in Fig. 6 shows a comparison of the BL profiles. The average roof velocity off the spoiler was 72% and 62% of the freestream for the full-scale (WT) and reduced-scale (WC) cases, respectively, with the BL height in the reduced regime being 85% thicker than the estimated full-scale thickness. Of interest, The displacement thickness and BL shape factor describe the development of the BL over the vehicle and provide information on the local environment of the BL itself at the measurement location. The displacement thickness, $\delta^*$, is measure of the effective height of the boundary layer. In addition, the shape factor, $H$, which is the ratio of the

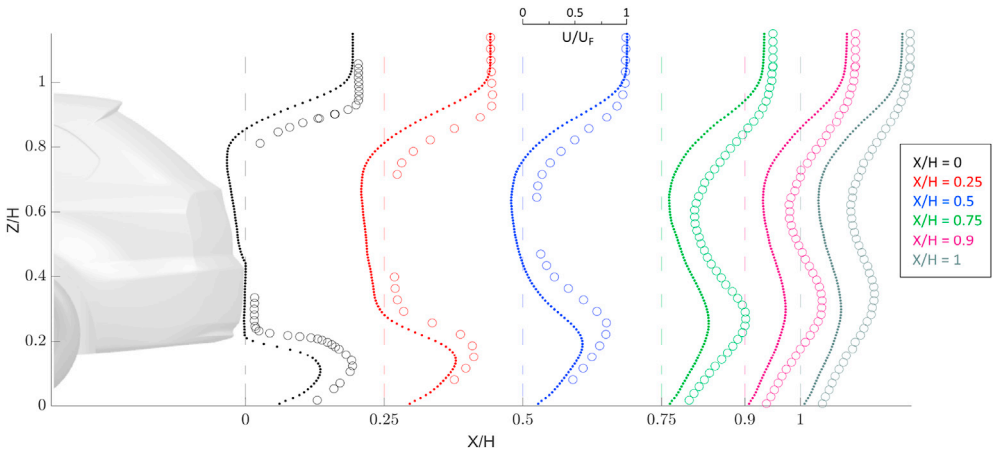


**Fig. 4.** Comparison of streamwise velocity profiles, $U/U_F$, at various longitudinal distances in the wake of the DrivAer estate vehicle. Hollow markers denote the full-scale results and solid dots are for the reduced scale.

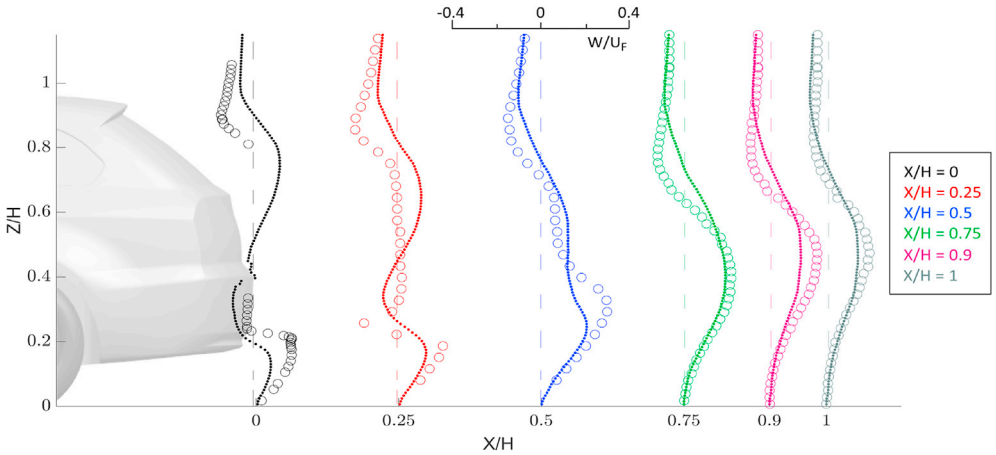


**Fig. 5.** Comparison of vertical velocity profiles, $W/U_F$, at various longitudinal distances in the wake of the DrivAer estate vehicle. Hollow markers denote the full-scale results and solid dots are for the reduced scale.

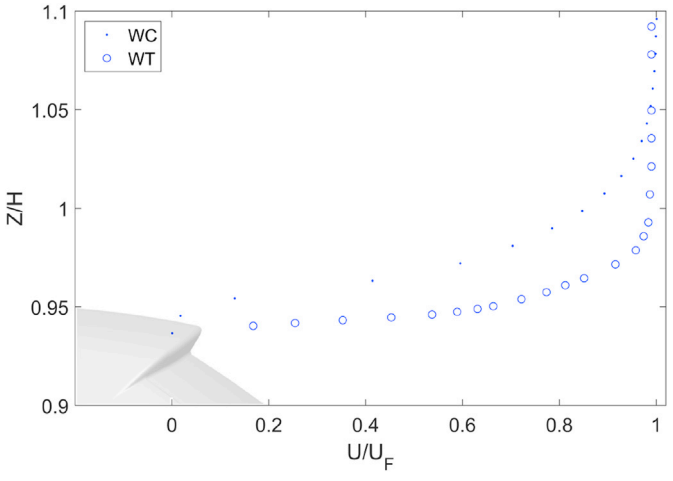


**Fig. 6.** Comparison of streamwise velocity, $U/U_F$, at the trailing edge of the roof spoiler for the full-scale (WT) and the reduced-scale cases (WC). The scale silhouette of the estate vehicle roof trailing edge is provided as reference.

displacement to momentum thickness, varies with pressure gradient and can act as a predictor of the early onset of turbulence and flow separation (Schlicting and Gersten, 2014). This is useful in understanding if the flow is in a developed and self-similar environment or subject to an adverse pressure gradient associated with decelerating flow. These quantities are defined as follows

$$\delta^* = \int_0^\infty \left(1 - \frac{U(y)}{U_F}\right) dy, \tag{1}$$

$$H = \frac{\delta^*}{\theta}, \tag{2}$$

with $\theta$, the momentum thickness, defined by

$$\theta = \int_0^\infty \frac{U(y)}{U_F}\left(1 - \frac{U(y)}{U_F}\right) dy. \tag{3}$$

The corresponding estimated displacement thicknesses for the separated roof shear layers are $0.012H$ (WT) and $0.033H$ (WC). The shape factors are 2.73 for the reduced-scale and 2.31 for the full-scale cases. This has two main implications for the roof flow characteristics. Firstly, both shape factors indicate that the flow over the roof is subject to a strong adverse pressure gradient. This is expected as the initially accelerated flow over the front windscreen should slow as it recovers and the roof slightly curves down towards the separation point. Secondly, the BL in the reduced-scale case is considerably thicker. This resultant reduction in momentum closer to the surface for the reduced-scale case helps explains the slower transport of momentum into the recirculation region of

the vehicle.

A key aspect for quantifying reduced Reynolds number effects for complex bluff body geometries is the flow behaviour around trailing edge radii. Presented in Figs. 7–9 are the streamwise velocity profiles of the separated shear layers in the proximity of three different geometric features of varying radii: the rear bumper, tail-lights and D-pillars. Of these, the tail-lights on the DrivAer have a 5 mm radius for the full-scale vehicle ($\sim 0.002W$), and thus can be treated similarly to a sharp corner such as the underbody exit or roof spoiler trailing edges.

At the rear bumper, at $Z/H = 0.3$, earlier separation is apparent for the reduced-scale case, with the velocity profiles approaching similarity downstream into the wake, as shown in Fig. 7. It is unknown if the large difference in the profiles at separation is solely due to the different boundary layer development or if flow associated with the wheel well is a large contributor.

Streamwise profiles at the tail-lights height of $Z/H = 0.5$ in Fig. 8 are effectively identical for the two cases, even with the influence of a wing mirror upstream. The estimated displacement thickness for both full-scale and reduced-scale cases were $0.0218H$ and $0.0223H$; a difference that can be considered trivial. Downstream of the separation point, the influence of the reduced Reynolds number on the diminished transport of momentum and convection towards the vehicle centreline is again noted, commonly present for all three geometric features.

For both cases at the D-pillar, a varying radii feature, Fig. 9 shows a small reduction in velocity further outboard, but the full-scale flow has a larger deficit close to the vehicle centreline, the inverse of flow around the rear bumper. Interestingly, this suggests the flow around the D-pillar remains attached for longer in the reduced scale case. At $X/H = 0.5$, the profiles are now similar in both cases.

Examination of the evolution of the streamwise trailing vortices from $X/H = 0.5$ to $X/H = 1$ in the wake are examined in Figs. 10 and 11. Despite recording $\sim 100\ St_{FA} = 0.2$ shedding cycles for the reduced-scale time-averaged results, clear asymmetry is present at both longitudinal locations, symmetry becoming more prominent further downstream. Comparison with the full-scale results show that the large-scale structures and the artefacts of flow off the wheels and wing mirrors are also captured at the reduced scale, with the rotational direction of the large streamwise structures consistent with the observation of strong upwash in the wake.

Whilst the size of the large streamwise structures ($A$) appear similar, the irregular shape in both regimes potentially suggests that this structure may not be a salient structure but rather be a time-averaged representation of vortex emissions from within the recirculation region. The

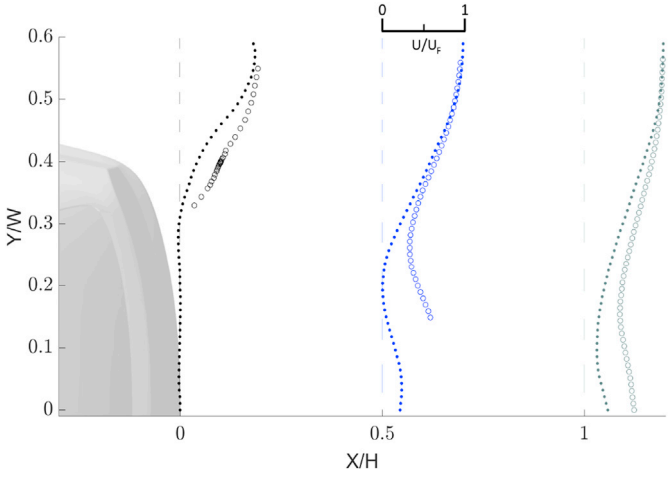


**Fig. 7.** Comparison of streamwise velocity, $U/U_F$, at the trailing edge of the rear bumper ($Z/H = 0.3$), between the two flow regimes at full-scale (WT, hollow markers) and the reduced regime (WC, solid markers). Dashed lines indicate the longitudinal measurement location.

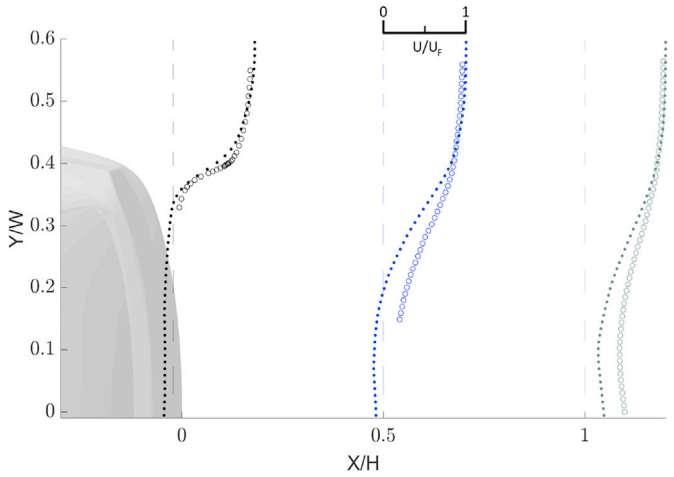


**Fig. 8.** Comparison of streamwise velocity, $U/U_F$, at the trailing edge of the tail-lights ($Z/H = 0.5$), between the two flow regimes at full-scale (WT, hollow markers) and the reduced regime (WC, solid markers). Dashed lines indicate the longitudinal measurement location.

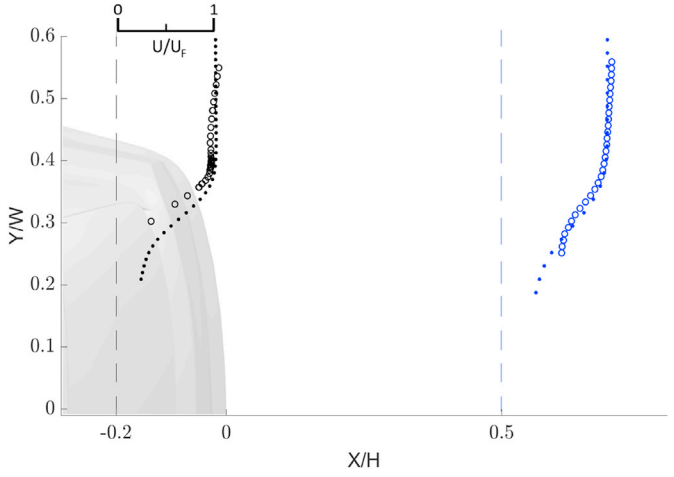


**Fig. 9.** Comparison of streamwise velocity, $U/U_F$, at the trailing edge of the D-pillar ($Z/H = 0.8$), between the two flow regimes at full-scale (WT, hollow markers) and the reduced regime (WC, solid markers). Dashed lines indicate the measurement location.

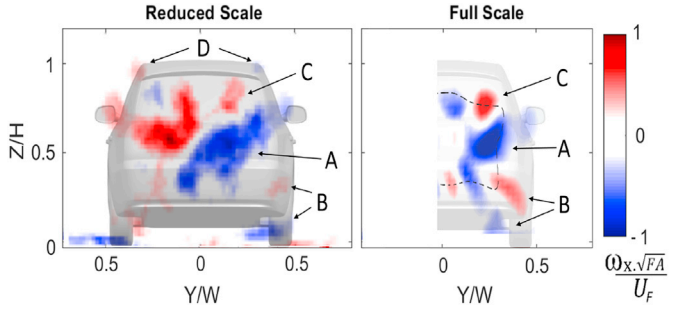


**Fig. 10.** Comparison of normalised streamwise vorticity, $U/U_F$, at the longitudinal distance of $X/H = 0.5$ for the full-scale and reduced-scale regimes. Full-scale results were acquired using a 4-hole dynamic pressure probe and reduced-scale results measured using PIV. Data at the full-scale within the dashed line indicates flow that was below the 80% acceptable data limit.

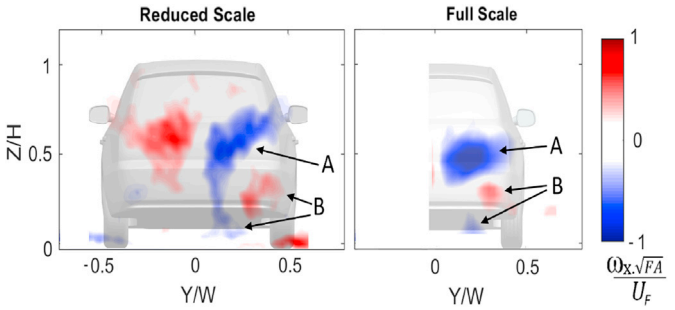


**Fig. 11.** Comparison of normalised streamwise vorticity, $U/U_F$, at the longitudinal distance of $X/H = 1$ for the full-scale and reduced-scale regimes. Full-scale results were acquired using a 4-hole dynamic pressure probe and reduced-scale results measured using PIV.

existence, formation and its nature in the transient flow is a topic of ongoing work and will be addressed in a future article. The pair of wheel jet vortex structures (*B*) appear to be captured in both flows and importantly, at similar locations in space, albeit the vortex structures being of higher strength in the full-scale regime. Vortex structure *C* is proposed to be the detached vortex structure off the D-pillar of the vehicle, consistent with the expected rotation direction and can be likened to a sedan vehicle's C-pillar vortex.

As the D-pillars are approximately angled 40° from the horizontal, the detachment bears similarities to the low-drag scenario of the Ahmed 30° or Ahmed 35° slant angle flow topology. An interesting flow feature that is not present at full scale are the A-pillar vortices (*D*) captured in the reduced-scale flow. At the downstream distance of $X/H = 1$, the main streamwise structure, *A*, remains dominant. These vortex structures in both cases maintain a similar height at both longitudinal distances and are slightly displaced inboard. The wheel jet vortices, *B*, remain at the reduced scale, although the cause for the relative increase in strength is currently unclear. The D-pillar structures are no longer distinct, their relative progression in vortex diffusion or cross-annihilation is consistent between the two cases.

The similarity between the two cases suggests that the lower Re PIV results can provide a more detailed interpretation of the higher Re estate wake. Streamlines along the vehicle centreline in Fig. 12 show a large lower recirculation structure from entrained flow exiting the underbody. The upper vortex is likely being represented as a roll-up of the roof shear layer with convection of reversed flow moving up the rear windscreen. Induced flow approaches the base of the vehicle and a bifurcation of the streamlines occurs at approximately $Z/H = 0.55$. A feature of the wake is that the length of the recirculation region (defined as the distance from the base to the furthest downstream location with negative streamwise velocity) is further downstream than the free stagnation point. This has

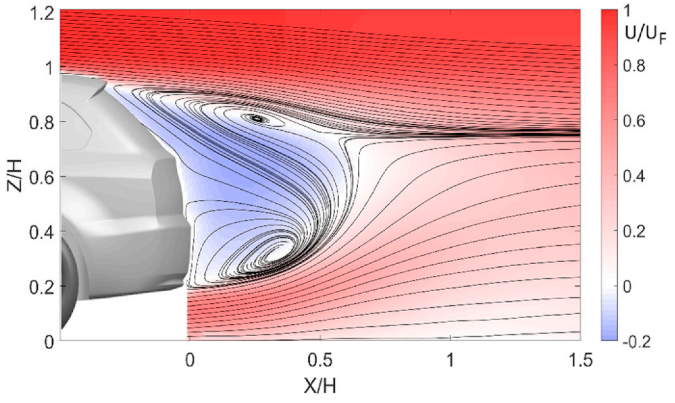


**Fig. 12.** Streamlines overlaid on a streamwise velocity contour, $U/U_F$ at the vehicle's symmetry plane, taken from reduced Reynolds number experiments.

been observed to similarly occur for the wakes of trucks (McArthur et al., 2016), despite the fact that the vortex cores are at approximately a similar downstream location for the wake of the estate.

When the reduced-scale results are analysed alongside previously attained full-scale base pressure surveys (Avadiar et al., 2018) shown in Fig. 13, several features of the proposed time-averaged wake are elucidated. The region of increased pressure at the middle of the base corresponds to a secondary stagnation of the reversed flow on the vehicle, likely induced by the lower vortex structure. Flow progresses up the base, separates at $Z/H = 0.6$ and reattaches onto the rear windscreen at $Z/H = 0.75$. Below the spoiler, a large pressure recovery is evident as the flow approaches stagnation.

Examination of the horizontal plane at $Z/H = 0.3$ in Fig. 14, shows strong lateral inboard flow is evident at the curved edge of the body, with a local minimum pressure corresponding to flow separation. Each side of the vehicle shows regions of alternating sign of vorticity, corresponding to the legs of a horseshoe vortex, or perhaps wheel jet vortices. As compared to Fig. 10, the transverse plane at $X/H = 0.5$ showed the outboard wheel vortex remains downstream of the body but the inboard vortex is close to the ground. Of interest, whilst the regions of vorticity

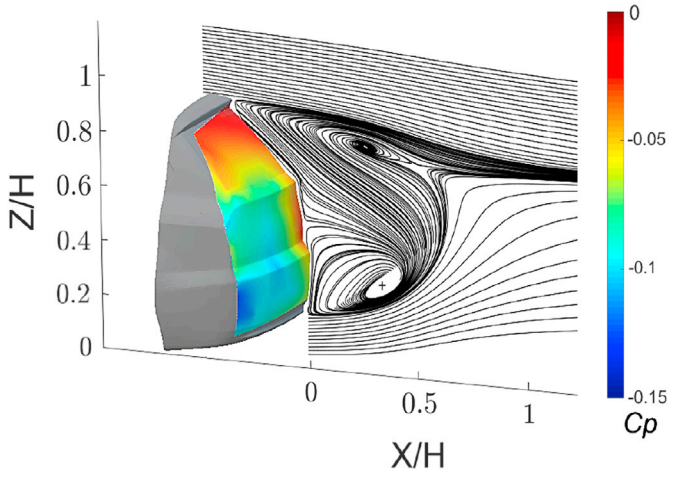


**Fig. 13.** Base pressure from full-scale experiments (Avadiar et al., 2018) overlaid with streamlines from reduced scale PIV at the vehicle's symmetry plane (as in Fig. 12).

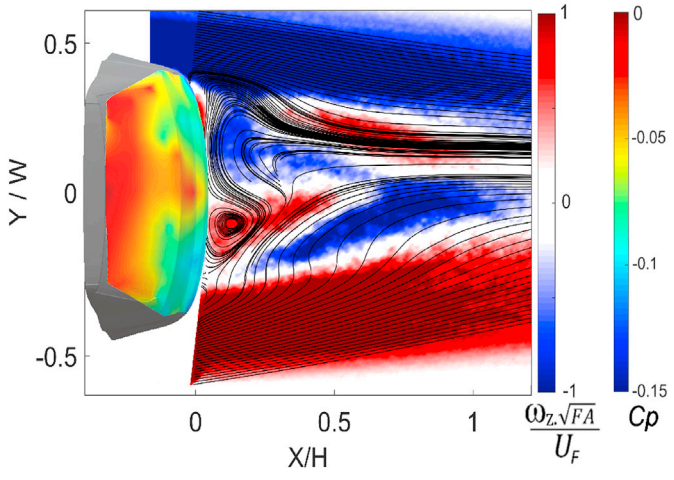


**Fig. 14.** Base pressure from full-scale experiments (Avadiar et al., 2018) overlaid with streamlines from reduced scale PIV at $Z/H = 0.3$ (rear bumper), coloured by normalised vorticity.

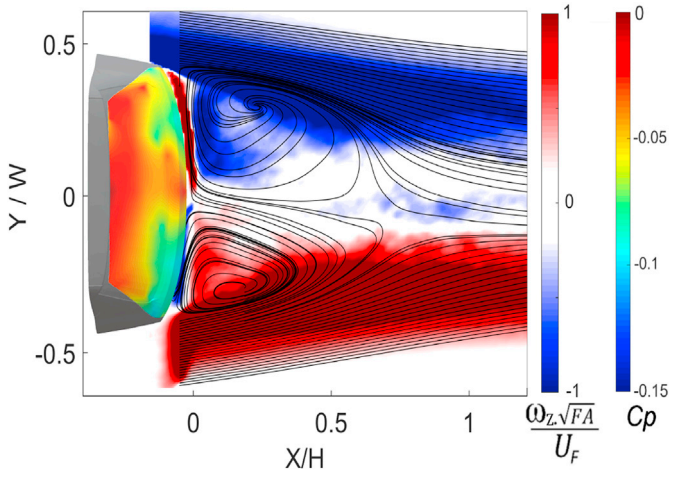


**Fig. 15.** Base pressure from full-scale experiments (Avadiar et al., 2018) overlaid with streamlines from reduced scale PIV at $Z/H = 0.5$ (tail-lights), coloured by normalised vorticity.

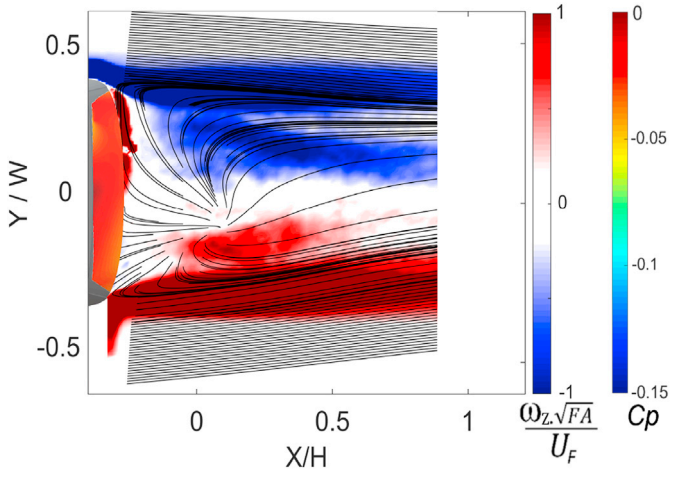


**Fig. 16.** Base pressure from full-scale experiments (Avadiar et al., 2018) overlaid with streamlines from reduced scale PIV at $Z/H = 0.8$ (D-pillar), coloured by normalised vorticity.

are largely symmetric about the vehicle's centreline, the streamlines depict an otherwise laterally biased wake, observed at $Z/H = 0.5$ and 0.8 (Fig 15 and Fig 16 respectively) as well. It is proposed that the wheel jet vortices on being convected along the underbody diffuser experience difference rates of expansion. The introduced asymmetry into the vehicle's wake, bears similarities to findings by Pavia and Passmore (2018) on the augmentation of the Windsor square-back wake from the presence of wheels.

At the mid-vehicle height of $Z/H = 0.5$, a clear left-right pair of vortices is evident. Additionally, these correspond to regions of low pressure on the base of the vehicle and appear to be dominant structures with vorticity magnitude comparable with the shear layers. As observed in Fig. 14, asymmetry is present in the wake with a larger bias observed for the streamlines than the vorticity. The skew of the wake however, is now biased towards the left of the vehicle, in contrast to the right bias at $Z/H = 0.3$.

### 3.2. Power spectra and transient properties

With similarities to the large-scale time-averaged wake observed, the nature and time-varying properties of the large-scale flow features between the two cases are of interest. This will primarily focus on the

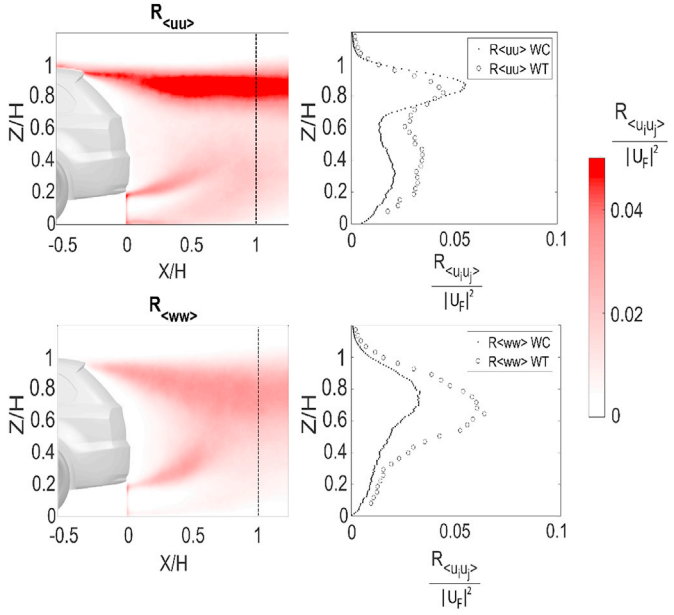


**Fig. 17.** Normalised principal Reynolds stresses, $R_{v'v'}$ and $R_{w'w'}$ for the reduced regime, WC (left) from the transverse plane at $X/H = 1$. The dashed line at $X/H = 1$ indicates the position where a comparison to complementary full-scale results, WT, is made (right). Full-scale results were measured using a 4-hole dynamic pressure probe with the reduced scale results obtained through PIV surveys.

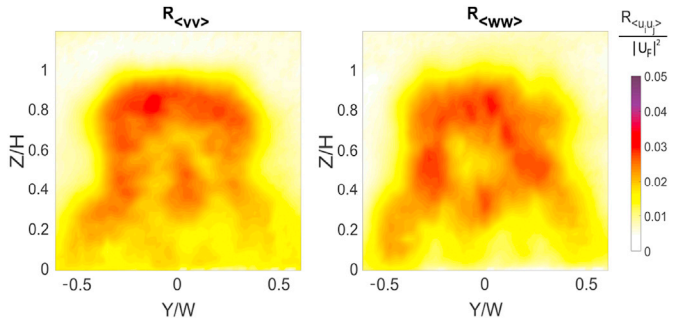


**Fig. 18.** Normalised principal Reynolds stresses, $R_{v'v'}$ and $R_{w'w'}$ for the reduced regime, WC calculated from PIV velocity measurements in the transverse plane at $X/H = 0.5$.

frequency content and magnitude of fluctuating velocities in the symmetry plane of the wake.

Before the specific spectra of the wake velocities is analysed, an examination of the normal Reynolds stresses is important to gauge the impact of turbulent diffusion. Fig. 17 depicts a highly turbulent roof shear layer and a relatively steady underbody exit flow for the streamwise normal stress. By $X/H = 1$ downstream, the turbulence level at the bottom shear layer from the underbody flow is diminished relative to the roof shear layer. The bias is noticeably less at full-scale for the upper and lower heights. Furthermore, the maximum magnitude of the vertical Reynolds stress, $\langle w'w' \rangle$, at full scale is slightly higher than its streamwise counterpart, the inverse occurring at the reduced scale. Furthermore, the vertical location of the wake closure height is estimated to be at $Z/H \sim 0.7$, a reduced height difference of $0.05H$ relative to the reduced scale.

Lateral and vertical principal Reynolds stresses, $R_{v'v'}$ and $R_{w'w'}$ from the transverse plane PIV measurements in the reduced regime are shown in Fig. 18. These suggest the primary fluctuations for both stresses are associated with the shear layers, with "legs" at $Z/H = 0.3$ at the outboard edge of the vehicle, likely tied to instabilities from the rear wheels. A

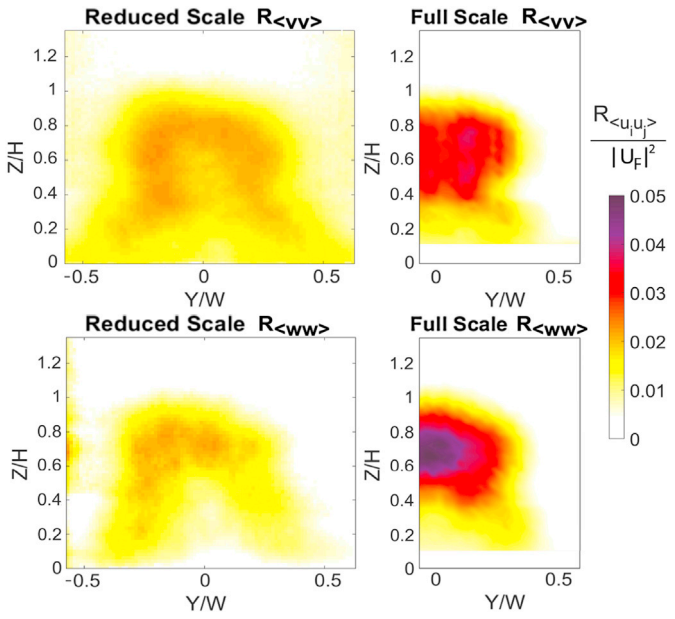


**Fig. 19.** Normalised principal Reynolds stresses, $R_{v'v'}$ and $R_{w'w'}$ for the reduced regime, WC (left) from the transverse plane at $X/H = 1$. Full-scale results (right) were measured using a 4-hole dynamic pressure probe with the reduced scale results obtained through PIV surveys.

peak exists at the centre of the lateral stress distribution; this is probably associated with the left-right oscillations of the vortex pair within the recirculation region shown previously in Fig. 15. Local regions of high magnitude in the vertical fluctuations at the vehicle centerline ($Z/H = 0.3$ and 0.8) are of the time-averaged lower and upper vortex structures, with similar peaks observed at the mid-plane height ($Y/W = \pm 0.25$) for the left-right pair of vortices. Of interest, the asymmetries observed at the horizontal and transverse planes are not clearly evident here.

Principal stresses downstream, $R_{v'v'}$ and $R_{w'w'}$, at $X/H = 1$ are shown in Fig. 19, with an expected reduction of fluctuation magnitude relative to full scale, but largely replicating the distribution. A small degree of asymmetry is present for both the vertical and lateral components, effectively offset by approximately $0.04W$. Both normal stresses display some skew, with the larger magnitudes biased toward the left side of the vehicle, with the vertical component, $R_{w'w'}$, being the most pronounced. Increased wheel jet vortex strength (Fig. 11), and the wake skew to the right of the vehicle (Fig. 14) at the height of the bumper ($Z/H = 0.3$), would result in the magnified expansion of the wake on the vehicle's left. Diffusion and breakdown of the vortex structures on the left side may be consequently accelerated, resulting in the increased fluctuation magnitudes.

An observed decrease in the underbody mean exit flow for the reduced regime relative to full scale, would explain its diminished magnitude of the biases observed. Increased momentum from the underbody flow exit would alternatively promote the consequential increased mixing of the two shear layers, to result in the increase of $\langle w'w' \rangle$. With vertical fluctuations for the full-scale case larger in magnitude than its streamwise counterpart, the more dominant vertical oscillations in the time-varying wake are potentially tied to stronger vertical oscillations of the free stagnation point.

To obtain a characteristic length scale of the typical structures from the roll-up of Kelvin-Helmholtz vortices within the roof shear layer, the auto-correlation length scale of the streamwise velocity was computed at $(X/H, Z/H) = (-0.1, 0.9)$. The auto-correlation method used the first zero-crossing method (O'Neill et al., 2004) on the fluctuating component of the streamwise velocity, $u'$. The integrated time period is then converted to a length scale by multiplying the local mean velocity. The time

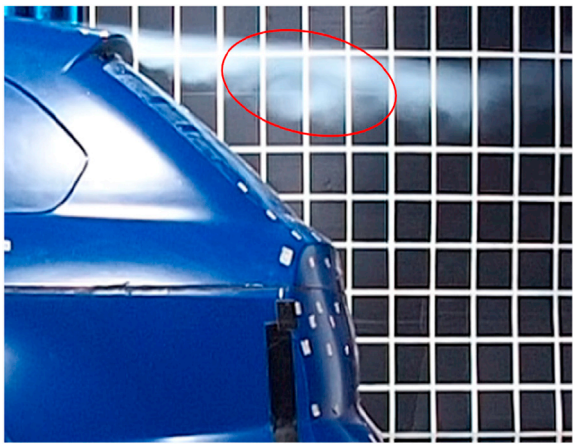

**Fig. 20.** Smoke flow visualization showing the roll-up of shear layer vortices in the wake. Smoke flow visualisation was conducted at $Re_L = 3\,000\,000$, with vortices within the downstream range of $X/H = -0.1$ to 0.1 considered when comparing to the auto-correlation length scale. The red ellipse highlights a sample of the shear-layer flow structures of interest. (For interpretation of the references to colour in this figure legend, the reader is referred to the Web version of this article.)

scale corresponded to a size of $0.09H$, comparing well to the full-scale value of $0.07H$. The local velocity at that location was used in determining the length scale. Comparing to smoke flow-visualization results in Fig. 20, the sizes were found to vary between 0.08 to $0.12H$ for 15 clear instances captured on video. Agreement was deemed to be good, especially when considering the subjective nature of measuring smoke flow structures and the difference in Reynolds number between the flow visualization experiments and velocity measurements .

Examination of autocorrelation length scales at $X/H = 1$ in Fig 21 depict good agreement between the two cases. Differences in the profiles are consistent with the streamwise velocity profiles presented in Fig. 4, corresponding to the residual flows from the underbody exit and roof shear layer. Interestingly, the seemingly uniform difference between the streamwise Reynolds stresses, $R_{u'u'}$, for the two cases are not transferable to length scale. By referring back to the streamwise velocity profiles, the largest variations occur due to the disparity in the positions of the local

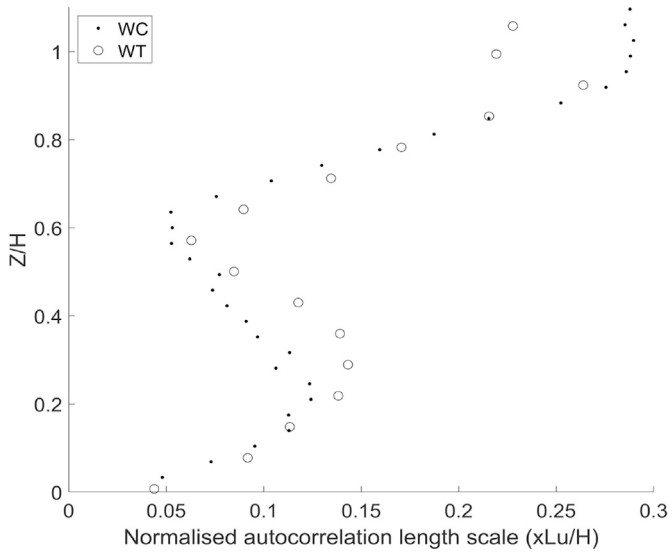


**Fig. 21.** Autocorrelation length scales (normalised by body height) of the streamwise velocity component $U/U_F$, calculated along the symmetry plane at $X/H = 1$. Solid dots denote the reduced-scale results (WC) and hollow markers refer to full-scale results (WT).

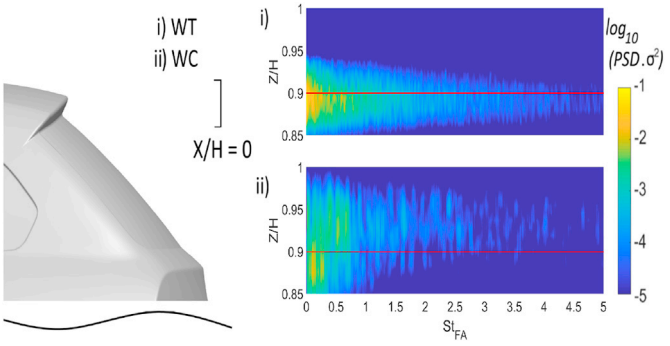


**Fig. 22.** Normalised PSD of the roof shear layer's streamwise velocity at $X/H = 0$ for the two regimes i) reduced scale – WC and ii) full scale – WT. The red line at $Z/H = 0.9$ represents the spectrum of the roof shear layer vortex roll-up auto-correlation length scale was computed. (For interpretation of the references to colour in this figure legend, the reader is referred to the Web version of this article.)

turning points. These locations are downstream artefacts of the underbody exit flow (maxima), and the maximum upwash or flow pitch from the recirculation region bounds (minima). The presence of larger scales from $Z/H = 0.3$ to 0.45 are likely associated with the transport of emissions from the lower recirculating vortex structure. Interestingly, at the height of $Z/H = 0.6$, the downstream region of the recirculation zone's maximum pitch, both Re cases have similar magnitudes of streamwise length scales. The small magnitude of these scales suggests that the rate of breakdown is still largely commensurate for both regimes, despite the different local velocities. The frequencies that these scales are associated with however, are likely to differ and this is examined later.

The inability to measure transient quantities within the recirculation region besides base pressures at full-scale limits the ability to readily compare the transient properties of the wake. However, the emission and breakdown of vortex structures further downstream may be considered a signature of the wake conditions upstream, providing insight into the downstream shear layers, vortex emission and wake closure properties.

The spectral content of the streamwise velocities in Fig. 22 for the roof shear layer at $X/H = 0$ shows a more broadband spectrum for the reduced Reynolds number regime. The peak ranges from $St_{FA} = 0.1$ to 1 in the reduced regime, in contrast to the more definitive $St_{FA} = 0.25$ to 1 at the full-scale.

Streamwise velocity spectra in Fig. 23 depict the roof shear layers with a wide peak between $St_{FA} = 0$ to 0.5 at the full-scale and with the

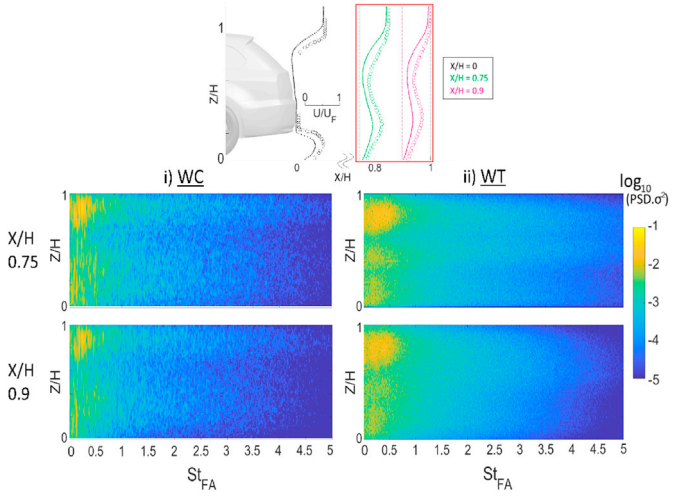


**Fig. 23.** Normalised PSD of the streamwise velocity, $U/U_F$, in the symmetry plane at $X/H = 0.75$ and 0.9 for the two regimes i) reduced scale – WC, and ii) full scale – WT.

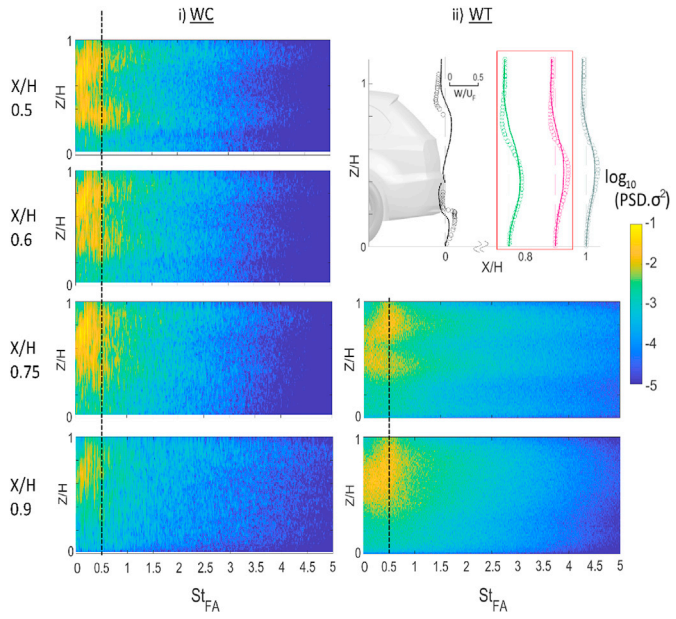


**Fig. 24.** Normalised PSD of the vertical velocity, $W/U_F$, in the symmetry plane at $X/H = 0.75$ and 0.9 for the two regimes i) reduced scale – WC, and ii) full-scale – WT.

reduced scale results indicating discernible frequencies present between $St_{FA} \approx 0.15$ and 0.3. Spectra at the heights below this region, for both Reynolds numbers, are noticeably weaker. The spatial distribution of frequencies relative to height reveals three bands present at $X/H = 0.75$ for the full-scale results only, becoming somewhat diminished at $X/H = 0.9$. This distribution of spectra agrees well with the reduced magnitude of fluctuating velocities at the lower heights based off the streamwise normal Reynolds stresses in Fig. 17. A close agreement between the two cases provides good confidence that future further transient analysis on the roof shear layer may yield information useful for control or passive modifications to the spoiler geometry.

Spectra of the vertical velocity, $W/U_F$, in Fig. 24, shows the energy content associated with the two shear layers for the lower Re flow converging on $Z/H = 0.75$ from the longitudinal distances of $X/H = 0.5$ to 0.9. At $X/H = 0.75$, two bands remain visible at full scale but becomes less evident for the reduced scale, only discernible by the decay. At $X/H = 0.9$, both regimes now clearly show a single band, with the reduced scale flow showing frequency peaks from $St_{FA} = 0.1$ to 0.3, compared to the broader range at full scale. As the spectra are normalised by the variance, the vertical velocity fluctuations at full scale may be associated with smaller-scale structures, either by transport or an artefact from mixing of the bottom and upper shear layers.

## 4. Conclusions

The influence of Reynolds number on the wake properties of the DrivAer estate have been presented. Time-averaged velocity profiles, frequency content and their derived quantities depict a similar wake state for flows differing by two orders of magnitude in Reynolds number. Large-scale flow structures and trends in velocity profiles are similarly represented in both cases. Smaller geometric features such as the wheels and wing mirrors maintain a similar influence on the wake properties, as observed in the streamwise vorticity. The wake of the estate in both cases remains dominated by upwash into the wake from the presence of an underbody diffuser. The streamwise structures present in the wake reflect this bias, with the rotation direction opposite to the classical C-pillar vortex structures observed in the literature for sedan type vehicles.

The lower Reynolds number alters the BL development around the vehicle. Shear-layer profiles under the influence of a pressure gradient or

associated with the curved trailing edge are clearly augmented. The underbody exit flow velocity magnitude and its resultant convection into the recirculation region show some differences between the two cases. However, downstream of the wake closure location, similar velocity profiles are observed. Base pressure contours from the full-scale correlates well with the PIV data acquired for the reduced-scale case, demonstrating the potential of elucidating properties of the full-scale flows using reduced-scale models.

Frequency spectra and normal stresses associated with the fluctuating flow exhibit similar properties between the two regimes, despite differences in the magnitudes and contributions of particular frequency components. The vertical position of the peak Reynolds Stress in the roof shear layer is higher in the low Re case, likely associated with the reduced underbody flow and, consequently, the increased momentum in the flow over the roof. In both Re cases, the highest fluctuating energy occurs in the roof shear layer. Downstream of the recirculation region, the reduced-scale wake contains more streamwise turbulence relative to its vertical component, as assessed by the Reynolds stress components.

The flow topology in the reduced Reynolds number experiments can be considered qualitatively similar in both their time-averaged and transient nature, but the derived or calculated drag is unlikely to be similar. Instead, the reduced-scale studies allow for the time-mean and transient behaviour of large-scale flow structures to be better understood, with implications for their contribution to drag. Augmentation of the surface geometry to reduce the sensitivity to Reynolds number through the addition of roughness was not utilised, due to the interactions between other upstream flow features such as mirrors, wheels and wheel wells that may present a greater influence. Ultimately, attempting to identify drag contributions or key frequencies of interest for control must still be conformed at a scale that can directly correlate back to the full-scale dynamics.

## Acknowledgements

The authors would like to thank the Ford Motor Company for access to the full-scale model used in this experimental study.

## References

Avadiar, T., Thompson, M., Sheridan, J., Burton, D., 2018. Characterisation of the wake of the drivaer estate vehicle. J. Wind Eng. Ind. Aerod. 177, 242–259.
Barry, N., Burton, D., Sheridan, J., Thompson, M., Brown, N., 2016. Flow field interactions between two tandem cyclists. Exp. Fluid 57 (181), 1–14.
Buresti, G., Fedeli, R., Ferraresi, A., 1997. Influence of afterbody rounding on the pressure drag of an axisymmetrical body. J. Wind Eng. Ind. Aerod. 69, 179–188.
Heft, A.I., Indinger, T., Adams, N., 2012. Introduction of a New Realistic Generic Car Model for Aerodynamic Investigations, Report. SAE International.
Li, C., Burton, D., Kost, M., Sheridan, J., Thompson, M., 2017. Flow topology of a container train wagon subjected to varying local loading configurations. New Results Numer. Exp. Fluid Mech. 3 169, 12–29.
Lienhart, H., Stoots, C., Becker, S., 2002. Flow and turbulence structures in the wake of a simplified car model. New Results Numer. Exp. Fluid Mech. 3 3, 323–330.
McArthur, D., Burton, D., Thompson, M., Sheridan, J., 2016. On the near wake of a simplified heavy vehicle. J. Fluid Struct. 66, 293–314.
Mousley, P., 2011. Flyercobraprobe. http://www.turbulentflow.com.au/Downloads/FlyerCobraProbe.pdf.
O'Neill, P., Nicolaides, D., Honnery, D., Soria, J., 2004. Autocorrelation Functions and the Determination of Integral Length with Reference to Experimental and Numerical Data. Australian Fluid Mechanics Conference.
Pavia, G., Passmore, M., 2018. Characterisation of wake bi-stability for a square-back geometry with rotating wheels. In: Wiedemann, J. (Ed.), Progress in Vehicle Aerodynamics and Thermal Management. Springer International Publishing, Cham, pp. 93–109.
Raffel, M., Willert, C., S, W., J, K., 2007. Particle Image Velocimetry: A Practical Guide, second ed. Springer, New York.
Schlicting, H., Gersten, K., 2014. Boundary Layer Theory, seventh ed. Springer.
Spohn, A., Gilliéron, P., 2002. Flow Separations Generated by a Simplified Geometry of an Automotive Vehicle.
Venning, J., LoJacono, D., Burton, D., Thompson, M., Sheridan, J., 2017. The nature of the vortical structures in the near wake of the ahmed body. J. Automob. Eng. 231, 1239–1244.
Wieneke, B., 2015. Piv uncertainty quantification from correlation statistics. Meas. Sci. Technol. 26 (7), 074002.
Williamson, C., 1996. Vortex dynamics in the cylinder wake. Annu. Rev. Fluid Mech. 28, 477–539.